THE ASTRONOMICAL JOURNAL, 119:44–58, 2000 January
© 2000. The American Astronomical Society. All rights reserved. Printed in U.S.A.

KINEMATICS AND MASS PROFILE OF AWM 7[1]

DANIEL M. KORANYI AND MARGARET J. GELLER
Harvard-Smithsonian Center for Astrophysics, 60 Garden Street, Cambridge, MA 02138; dkoranyi@cfa.harvard.edu, mgeller@cfa.harvard.edu
Received 1999 June 24; accepted 1999 September 30

ABSTRACT

We have measured 492 redshifts (311 new) in the direction of the poor cluster AWM 7 and have identified 179 cluster members (73 new). We use two independent methods to derive a self-consistent mass profile, under the assumptions that the absorption-line galaxies are virialized and that they trace an underlying Navarro, Frenk, & White (NFW) dark matter profile: (1) we fit such an NFW profile to the radial distribution of galaxy positions and to the velocity dispersion profile; (2) we apply the virial mass estimator to the cluster. With these assumptions, the two independent mass estimates agree to $\sim 15\%$ within 1.7 h^{-1} Mpc, the radial extent of our data; we find an enclosed mass $\sim(3 \pm 0.5) \times 10^{14}\ h^{-1}\ M_{\odot}$. The largest potential source of systematic error is the inclusion of young emission-line galaxies in the mass estimate. We investigate the behavior of the surface term correction to the virial mass estimator under several assumptions about the velocity anisotropy profile, still within the context of the NFW model, and remark on the sensitivity of derived mass profiles to outliers. We find that one must have data out to a large radius in order to determine the mass robustly, and that the surface term correction is unreliable at small radii.

Key words: galaxies: clusters: individual (AWM 7) — galaxies: kinematics and dynamics

1. INTRODUCTION

The properties of galaxy clusters play an important role in constraining cosmological parameters and models of large-scale structure formation. Because clusters are the most massive collapsed aggregates in the universe, the cluster mass function and its evolution with redshift constrains the spectrum of density fluctuations (e.g., Eke, Cole, & Frenk 1996; Bahcall & Cen 1992). Accurate cluster masses can also constrain the ratio of baryonic to total mass, and thus Ω_0 (White et al. 1993).

There are several standard ways of computing cluster masses. Optical redshift surveys yield a mass estimate through the application of the virial theorem, on the assumption that the galaxies trace the overall cluster mass distribution; this method was first applied to Coma by Zwicky (1933). More sophisticated variants of this method include a surface term to account for the unsampled portion of the cluster (The & White 1986) and use the Jeans equation to account for the effects of orbital anisotropy (e.g., Binney & Tremaine 1987). For clusters with many hundreds of redshifts, the distribution of infalling galaxies in redshift space measures the gravitational potential of the dark matter halo (Diaferio & Geller 1997); this method has so far been successfully applied only to Coma (Geller, Diaferio, & Kurtz 1999). Observations of hot intracluster gas in the X-ray provide information about the gravitational potential; the added assumption of hydrostatic equilibrium yields a mass (Bahcall & Sarazin 1977). Gravitational lensing of background galaxies can also be used to estimate cluster masses (Webster 1985; Bartelmann et al. 1996, and references therein). Comparing cluster masses derived by these independent methods can provide insight into the internal structure of clusters (Loeb & Mao 1994) and provides a consistency check on the mass derived by any one method.

While the distribution of total cluster masses constrains global cosmological parameters, knowledge of the density (or, equivalently, mass) profiles of individual clusters constrains models of cluster formation. *N*-body simulations of hierarchical clustering by Navarro, Frenk, & White (1995, 1996, 1997, hereafter NFW) suggest that a universal two-parameter density model can adequately describe clusters over a broad range of masses. Until recently, few clusters had enough measured redshifts to constrain the mass profile; the advent of multifiber spectrographs has now made it possible to measure several hundred redshifts in a cluster within a reasonable time.

Our goal is to measure the mass profile of the cluster AWM 7, selected by Albert, White, & Morgan (1977) on the basis of the cD galaxy at its center. Our sample consists of 179 cluster galaxies with measured redshifts; this work expands the sample of Koranyi et al. (1998) by 70%, extending the surveyed region to a projected radius of 1.7 h^{-1} Mpc and reaching fainter magnitudes in the core. We confirm the cold core seen in Koranyi et al. (1998) and fit an NFW mass profile from the projected distribution of radii for comparison with the virial mass profile; we consider also the effect of orbital anisotropies (still assuming the NFW profile) on the mass estimates. The two profiles agree remarkably well within our restricted context; the assumption of the NFW model produces self-consistent mass estimates using these two methods. Relaxing the assumption that the galaxies trace an underlying NFW dark matter distribution would result in a larger range of admissible masses (cf. The & White 1986).

In §§ 2 and 3, we describe the observations and data reduction. In § 4 we describe the data, and in § 5 we justify the choice of the NFW model, compute the resultant mass profiles, and comment on the reliability of the surface term correction. We defer discussion of some details until § 6 and

[1] Observations reported in this paper were obtained at the Multiple Mirror Telescope Observatory, a facility operated jointly by the University of Arizona and the Smithsonian Institution; at the Whipple Observatory, a facility operated jointly by the Smithsonian Astrophysical Observatory and Harvard University, and at the WIYN Observatory, a joint facility of the University of Wisconsin-Madison, Indiana University, Yale University, and the National Optical Astronomy Observatories.

conclude in § 7. We use $H_0 = 100\ h$ km s^{-1} Mpc^{-1} throughout.

2. OBSERVATIONS

We observed a total of 593 distinct targets in the direction of AWM 7 from 1995 to 1999. We measured redshifts for 492 objects; 179 are cluster galaxies (with redshifts in the range 2500–7500 km s^{-1}), making AWM 7 one of the best-sampled clusters in the sky. Our sample extends over 1°.5 in radius from the cluster center and reaches magnitudes as faint as $R = 18$ in the core. We collected data from three different telescopes, with different sky coverage and different magnitude limits; we describe the details of each in turn. In each case we chose the spectral coverage so that both the Ca H-K break at $\lambda\lambda$3933, 3968 and Hα λ6562 would fall on the detector at the cluster redshift. These spectral features are important for determining redshifts by cross-correlation with template spectra. We list the redshifts for all measured objects in Table 1.

2.1. *FAST Observations*

We used the FAST Spectrograph (Fabricant et al. 1998) mounted on the 1.5 m Tillinghast telescope at the Fred Lawrence Whipple Observatory on Mount Hopkins to observe 302 targets over $\sim$10 deg^2 of sky centered on NGC 1129. We selected the targets from the Digitized Palomar Observatory Sky Survey scans. We used a 3″ slit and a 300 line mm^{-1} grating, resulting in a resolution of $\sim$6 Å and spectral coverage of 3600–7600 Å. FAST can reliably measure redshifts for galaxies down to $R \sim 15.5$ and can measure redshifts for galaxies as faint as $R \sim 16$ if the central surface brightness is sufficiently high. 159 FAST targets are new to this paper; 51 of these are cluster members.

2.2. *MMT Observations*

We observed 45 targets with the Blue Channel spectrograph of the MMT on the nights of 1996 December 5 and 6, using a 2″ slit and a 300 line mm^{-1} grating, resulting in a resolution of $\sim$10.6 Å and spectral coverage of 3000–8000 Å. These targets are in the central 75′ × 75′ (1.15 h^{-1} × 1.15 h^{-1} Mpc) of the cluster and are complete to $R = 16.5$ in that region. These data have been previously published in Koranyi et al. (1998).

2.3. *Hydra Observations*

We observed 250 targets (under the queue observing scheme) with the Hydra multifiber bench spectrograph mounted on the Wisconsin-Indiana-Yale-NOAO (WIYN) telescope at Kitt Peak on the nights of 1998 December 20 and 21; these data are new to this paper. There were four separate fiber configurations; 60 objects were observed in more than one configuration. There were either four or five 25 minute exposures for each configuration. We used 3″ fibers and a 400 line mm^{-1} grating, resulting in a resolution of $\sim$7 Å and spectral coverage of 3800–7000 Å. The four configurations were observed under strongly varying conditions, resulting in dramatic differences in throughput. Two of the configurations suffered from wind shake, and a third from cirrus. The remaining configuration was observed under stable, clear skies with good seeing and resulted in a redshift for almost every target.

In total, we were able to measure redshifts for 154 of the 250 targets (152 new), sometimes by combining spectra of

TABLE 1

REDSHIFTS OF TARGET GALAXIES

α_{2000}	δ_{2000}	cz (km s^{-1})	σ_{cz} (km s^{-1})	Spectral Type
02 45 12.81	+41 44 04.6	4970	49	Ab
02 45 27.99	+41 28 28.5	11316	66	Em
02 45 31.82	+40 58 54.7	8327	21	Ab
02 45 31.90	+41 14 34.3	5127	51	Ab
02 45 32.39	+42 09 27.6	5546	18	Em
02 45 32.70	+41 33 46.5	3768	67	Em
02 45 32.87	+42 11 48.4	9677	67	Em
02 45 36.34	+42 09 27.3	5063	22	Ab
02 45 39.40	+42 01 46.4	10950	66	Em
02 45 43.58	+42 18 12.3	18849	67	Em
02 45 43.68	+42 00 38.1	11078	27	Em
02 45 44.96	+41 43 57.5	9637	67	Em
02 45 46.25	+41 13 43.6	8298	21	Ab
02 45 54.30	+41 50 22.9	33947	26	Ab
02 45 59.29	+41 19 18.7	5316	19	Ab
02 45 59.74	+42 32 32.3	11585	28	Ab
02 46 00.96	+42 51 08.4	36770	34	Em
02 46 01.34	+40 05 23.5	8965	25	Em
02 46 02.79	+40 05 35.5	8529	69	Em
02 46 05.21	+41 56 13.1	31731	68	Em
02 46 05.33	+42 06 05.7	3955	67	Em
02 46 08.10	+41 28 36.5	18682	35	Ab
02 46 10.37	+41 38 07.8	8733	48	Em
02 46 13.36	+42 25 04.4	11563	31	Ab
02 46 15.39	+42 24 22.1	11604	32	Ab
02 46 17.58	+42 37 44.9	11150	33	Em
02 46 18.47	+40 51 56.4	30809	39	Ab
02 46 24.61	+41 16 36.6	4672	34	Ab
02 46 26.90	+41 24 18.8	23942	37	Ab
02 46 27.10	+42 37 40.7	11229	66	Em
02 46 35.73	+42 10 44.8	9598	67	Em
02 46 42.41	+42 38 53.5	11202	18	Em
02 46 46.75	+42 06 59.5	10031	66	Em
02 46 47.95	+42 02 27.1	8322	67	Em
02 46 48.14	+41 30 32.0	23566	22	Em
02 46 54.08	+42 40 14.1	11233	29	Ab
02 46 57.12	+41 59 15.6	5098	38	Ab
02 46 58.13	+42 58 49.5	5411	67	Em
02 46 58.43	+41 46 33.3	4628	23	Ab
02 47 01.76	+41 39 07.3	10482	66	Em
02 47 14.32	+41 38 28.8	6028	68	Em
02 47 18.94	+41 32 29.8	31228	32	Ab
02 47 25.68	+42 59 56.0	8064	50	Em
02 47 26.11	+41 01 35.6	31070	36	Ab
02 47 31.63	+42 57 17.5	19454	68	Em
02 47 33.25	+42 37 53.2	31893	37	Em
02 47 40.54	+40 29 42.0	5607	32	Ab
02 47 49.16	+41 12 44.2	4126	16	Em
02 47 55.08	+42 12 16.7	5988	66	Em
02 47 56.33	+41 14 49.2	4035	67	Em
02 47 56.79	+41 20 55.1	32693	26	Em
02 47 57.73	+40 18 29.9	4985	22	Ab
02 47 58.14	+41 19 23.9	4855	47	Ab
02 48 02.17	+40 47 46.2	5154	66	Em
02 48 02.29	+43 02 02.0	11301	24	Ab
02 48 17.12	+41 09 49.2	5090	30	Ab
02 48 22.03	+41 36 47.2	5217	23	Ab
02 48 41.31	+42 59 27.3	30856	28	Em
02 48 49.65	+40 40 46.4	5219	19	Ab
02 48 53.77	+41 46 40.3	8359	32	Ab
02 48 59.01	+41 02 21.1	5169	43	Ab
02 49 09.34	+41 34 57.8	4686	24	Ab
02 49 09.55	+41 34 47.7	4698	22	Ab
02 49 10.32	+40 27 40.8	8914	27	Ab

TABLE 1—*Continued*

α_{2000}	δ_{2000}	cz (km s^{-1})	σ_{cz} (km s^{-1})	Spectral Type
02 49 19.27	+42 11 38.8	9674	16	Em
02 49 20.60	+40 53 17.0	4160	31	Ab
02 49 25.44	+42 53 27.3	19527	33	Em
02 49 32.66	+40 33 04.3	9007	67	Em
02 49 40.90	+41 03 17.0	5488	31	Ab
02 49 45.30	+42 22 05.8	19810	68	Em
02 49 45.90	+41 27 26.1	24086	44	Em
02 49 46.10	+41 03 06.0	6107	67	Em
02 49 48.10	+41 27 45.5	5279	17	Ab
02 49 50.18	+42 32 56.8	9311	67	Em
02 49 51.00	+41 34 03.7	5999	29	Ab
02 49 55.11	+40 28 54.7	27720	50	Ab
02 49 57.80	+40 43 28.3	7275	68	Em
02 49 59.40	+42 30 53.7	6823	70	Em
02 50 01.50	+40 20 57.1	9002	19	Em
02 50 03.48	+43 00 09.5	5052	45	Ab
02 50 03.51	+40 04 47.9	17920	32	Ab
02 50 04.50	+41 23 23.1	5765	38	Em
02 50 26.50	+41 56 45.4	5013	28	Em
02 50 33.80	+41 52 45.3	4159	50	Ab
02 50 38.90	+41 41 54.5	4281	22	Ab
02 50 40.70	+41 40 18.3	4336	67	Em
02 50 41.11	+40 28 49.1	8689	67	Em
02 50 41.70	+42 00 21.1	4000	67	Em
02 50 44.81	+40 04 10.7	18109	43	Ab
02 50 47.66	+40 18 44.1	16927	67	Em
02 50 48.82	+40 06 16.9	18140	28	Ab
02 50 52.80	+41 45 52.7	5449	62	Ab
02 50 55.60	+41 37 59.9	4614	13	Em
02 50 58.30	+41 03 42.8	3566	68	Em
02 51 03.55	+42 12 21.4	50965	58	?
02 51 04.19	+40 10 56.9	8817	33	Ab
02 51 04.29	+41 41 42.3	39801	63	Ab
02 51 04.94	+41 42 06.8	23973	36	Ab
02 51 07.36	+42 11 12.6	51068	50	?
02 51 12.58	+41 02 09.4	8995	19	Ab
02 51 12.80	+40 59 35.5	6229	68	Em
02 51 15.72	+42 13 04.3	50820	45	?
02 51 17.20	+42 07 03.8	3898	72	Em
02 51 17.70	+41 09 18.4	3433	21	Ab
02 51 18.60	+41 33 55.1	5733	34	Ab
02 51 19.02	+41 16 37.5	21307	62	Ab
02 51 20.56	+40 16 03.1	16937	14	Em
02 51 23.90	+41 57 33.6	3255	67	Em
02 51 26.71	+40 07 36.6	8868	29	Ab
02 51 28.01	+41 33 36.0	28088	91	Ab
02 51 29.30	+40 44 26.8	8095	25	Ab
02 51 31.37	+41 17 57.0	20545	31	Em
02 51 33.50	+40 46 27.1	41289	40	Ab
02 51 33.67	+41 41 29.3	50262	71	Ab
02 51 34.50	+40 43 53.4	8899	36	Ab
02 51 34.80	+40 06 46.7	9059	39	Ab
02 51 36.35	+41 22 56.1	9508	20	Ab
02 51 37.80	+40 44 24.1	8077	18	Em
02 51 38.65	+40 58 33.0	22112	67	Ab
02 51 39.58	+42 09 07.7	24829	21	Em
02 51 41.10	+42 21 52.0	11191	68	Em
02 51 42.80	+42 24 09.0	11311	67	Em
02 51 43.22	+42 49 43.4	5420	33	Ab
02 51 44.51	+42 07 45.4	32976	58	Ab
02 51 45.05	+41 23 15.5	11360	72	Em
02 51 51.10	+41 33 21.3	5241	54	Em
02 51 52.26	+41 30 38.9	4324	67	Ab
02 51 53.20	+41 45 28.2	61	32	star
02 51 56.67	+42 03 13.7	14286	66	Em
02 51 58.22	+40 08 29.8	8954	32	Em

TABLE 1—*Continued*

α_{2000}	δ_{2000}	cz (km s^{-1})	σ_{cz} (km s^{-1})	Spectral Type
02 52 00.40	+40 42 07.8	18137	38	Ab
02 52 00.60	+41 27 12.0	−103	17	star
02 52 07.90	+41 34 45.9	4572	17	Ab
02 52 08.60	+41 14 47.3	23852	37	Ab
02 52 15.33	+41 50 30.9	46155	29	Ab
02 52 15.50	+41 23 55.1	5835	24	Ab
02 52 15.64	+41 20 01.2	39268	64	Ab
02 52 16.99	+41 23 44.4	17073	21	Ab
02 52 19.90	+42 12 50.6	−119	40	star
02 52 22.98	+42 55 15.0	19442	27	Ab
02 52 25.90	+41 53 00.9	8618	70	Em
02 52 26.38	+42 05 48.7	3650	67	Em
02 52 32.51	+41 03 02.8	87281	59	Ab
02 52 33.87	+41 21 48.9	5340	45	Ab
02 52 34.22	+43 10 02.3	15544	71	Em
02 52 36.46	+42 08 46.3	50559	74	Ab
02 52 38.50	+41 34 41.1	4618	20	Ab
02 52 39.17	+41 36 55.7	19436	55	Ab
02 52 39.80	+42 08 52.3	31134	67	Em
02 52 40.40	+41 23 46.5	3963	66	Em
02 52 42.00	+41 48 48.6	34212	15	Em
02 52 42.30	+41 19 33.5	4471	54	Ab
02 52 43.10	+41 06 08.8	5957	31	Ab
02 52 43.26	+43 07 49.4	15720	18	Em
02 52 44.57	+41 00 07.7	4076	70	Em
02 52 44.65	+41 01 02.2	31238	30	Em
02 52 45.00	+42 09 44.9	32899	33	Ab
02 52 45.07	+42 10 15.9	31340	48	Ab
02 52 46.00	+41 00 22.1	30922	33	Ab
02 52 51.20	+42 12 18.1	3655	18	Em
02 52 51.95	+41 26 21.3	5725	73	Ab
02 52 52.43	+42 09 16.2	9623	67	Em
02 52 54.48	+41 40 18.0	5363	73	Em
02 52 55.64	+43 08 10.1	15681	36	Ab
02 52 55.86	+41 34 29.4	31111	71	Ab
02 52 56.30	+40 31 12.5	16466	19	Em
02 52 58.90	+41 32 01.6	6770	25	Ab
02 52 59.00	+41 27 14.6	34196	64	Ab
02 52 59.00	+41 58 24.7	5387	26	Ab
02 53 00.70	+41 06 27.0	9178	72	Em
02 53 00.70	+42 06 24.6	46141	58	Ab
02 53 00.80	+40 50 23.6	9154	32	Em
02 53 03.13	+42 00 43.9	76865	72	Ab
02 53 03.50	+41 17 25.8	14376	68	Em
02 53 03.77	+42 51 12.2	9466	67	Em
02 53 03.86	+41 42 00.6	523	82	Em
02 53 05.60	+41 19 39.3	56881	55	Ab
02 53 05.61	+41 04 27.9	4936	24	Ab
02 53 06.31	+42 12 08.0	19684	45	Ab
02 53 07.00	+41 12 37.9	15993	69	Em
02 53 07.62	+42 02 41.6	18748	67	Em
02 53 07.70	+41 25 03.7	5613	32	Ab
02 53 10.26	+41 47 08.9	18947	83	Em
02 53 10.74	+41 36 29.8	51527	63	Ab
02 53 11.62	+41 33 42.6	50888	46	Ab
02 53 13.08	+41 34 28.7	50600	61	Ab
02 53 13.59	+42 55 44.2	19562	36	Ab
02 53 14.10	+41 45 21.6	50734	45	Ab
02 53 16.05	+42 01 43.1	23527	75	Ab
02 53 16.20	+41 29 11.8	5262	26	Ab
02 53 16.24	+41 27 22.7	23987	45	Ab
02 53 16.80	+41 27 58.2	23927	38	Ab
02 53 17.18	+41 20 56.7	3703	80	Em
02 53 18.52	+41 25 56.4	23822	74	Em
02 53 20.75	+41 56 48.3	5440	37	Ab
02 53 20.93	+41 23 52.2	26527	32	Ab

TABLE 1—*Continued*

α_{2000}	δ_{2000}	cz (km s^{-1})	σ_{cz} (km s^{-1})	Spectral Type
02 53 20.93	+42 34 58.0	19312	31	Ab
02 53 22.03	+43 11 28.7	15598	68	Em
02 53 25.20	+42 08 01.5	68016	80	Em
02 53 25.54	+42 39 31.8	19693	19	Em
02 53 26.28	+41 56 35.2	5338	44	Ab
02 53 27.81	+41 26 32.6	23640	68	Em
02 53 27.90	+40 42 25.1	18364	36	Em
02 53 29.00	+42 05 06.4	41114	44	Em
02 53 30.00	+41 39 03.4	4840	32	Ab
02 53 34.01	+43 00 17.5	23252	66	Em
02 53 34.60	+41 53 08.1	7298	66	Em
02 53 36.30	+42 18 13.7	6599	67	Em
02 53 40.00	+42 01 00.5	41059	51	Ab
02 53 40.20	+41 43 31.1	6290	28	Ab
02 53 42.47	+41 58 21.0	60996	121	Ab
02 53 44.10	+41 27 15.1	4010	32	Ab
02 53 47.10	+41 32 49.1	5161	31	Ab
02 53 50.00	+41 27 18.4	4616	44	Ab
02 53 51.30	+41 43 38.2	5256	18	Ab
02 53 51.80	+41 55 42.8	56190	77	Em
02 53 52.85	+41 48 42.2	39792	42	Ab
02 53 53.56	+41 52 40.1	41957	63	Ab
02 53 54.50	+41 40 25.6	5561	49	Ab
02 53 56.13	+41 10 06.8	39013	46	Ab
02 53 57.13	+42 57 39.2	18221	67	Em
02 53 59.50	+41 47 35.1	6324	23	Ab
02 54 03.19	+42 13 03.4	19372	72	Em
02 54 03.46	+41 33 29.0	6107	50	Ab
02 54 05.72	+41 57 44.9	4331	43	Ab
02 54 05.74	+41 31 04.5	16986	82	Em
02 54 06.70	+42 01 14.8	17173	26	Em
02 54 08.93	+42 04 04.1	45918	77	Em
02 54 11.80	+40 58 46.4	9175	71	Ab
02 54 11.97	+42 32 51.5	14978	67	Em
02 54 12.28	+41 51 17.2	41741	53	Ab
02 54 14.80	+41 23 00.0	6413	17	Ab
02 54 16.40	+41 39 38.4	5150	30	Ab
02 54 16.53	+42 43 33.3	6357	66	Em
02 54 16.98	+41 34 52.3	5477	55	Ab
02 54 18.43	+42 12 26.8	51290	65	Ab
02 54 23.17	+42 08 03.3	23435	72	Em
02 54 23.43	+41 34 25.3	−46	16	star
02 54 23.84	+41 31 21.2	50504	61	Ab
02 54 24.12	+41 34 31.6	−142	48	star
02 54 24.40	+41 36 19.4	6129	26	Ab
02 54 24.66	+41 34 37.4	−122	16	star
02 54 25.30	+41 34 35.9	5085	16	Ab
02 54 26.21	+42 39 00.8	2193	67	Em
02 54 26.85	+41 39 19.3	5700	11	Ab
02 54 26.90	+41 39 19.6	−1	0	star
02 54 27.40	+41 30 47.3	4827	73	Ab
02 54 27.50	+41 34 42.5	5288	71	Ab
02 54 27.92	+41 32 23.6	50077	35	Ab
02 54 28.56	+41 35 58.0	5272	41	Ab
02 54 28.57	+41 26 55.9	4905	22	Ab
02 54 29.04	+41 10 07.6	4528	39	Ab
02 54 29.15	+41 50 35.3	50943	89	Em
02 54 30.37	+41 56 32.8	41025	91	Em
02 54 30.40	+41 36 36.2	6230	24	Ab
02 54 31.52	+41 25 04.5	24013	74	Em
02 54 32.20	+41 26 11.9	19755	41	Ab
02 54 32.40	+42 23 41.2	23731	38	Em
02 54 33.30	+41 23 48.3	19365	55	Ab
02 54 34.01	+41 33 31.3	5351	17	Ab
02 54 34.19	+41 59 17.4	40644	88	Ab
02 54 36.00	+41 53 25.0	5407	22	Ab

TABLE 1—*Continued*

α_{2000}	δ_{2000}	cz (km s^{-1})	σ_{cz} (km s^{-1})	Spectral Type
02 54 38.30	+41 35 18.1	5645	26	Ab
02 54 39.25	+42 09 36.9	6101	16	Ab
02 54 40.00	+41 34 31.1	5006	39	Ab
02 54 41.40	+41 33 49.3	5291	45	Ab
02 54 43.18	+41 49 50.8	50221	85	Em
02 54 43.66	+41 24 48.6	56323	50	Ab
02 54 44.00	+41 39 18.0	5372	25	Ab
02 54 44.10	+41 52 08.8	5974	24	Ab
02 54 44.60	+41 31 41.4	4450	22	Ab
02 54 45.71	+41 46 53.2	45951	57	Ab
02 54 47.60	+41 18 50.0	5904	40	Ab
02 54 48.10	+41 24 34.0	5622	16	Ab
02 54 49.80	+41 37 25.4	5994	38	Ab
02 54 51.64	+40 58 14.7	71647	54	Ab
02 54 54.14	+43 09 26.1	9138	67	Em
02 54 54.67	+41 23 20.0	56455	51	Ab
02 54 55.13	+41 30 48.0	72	33	star
02 54 55.30	+41 24 15.4	5423	42	Ab
02 54 55.83	+41 10 49.7	18262	72	Em
02 54 56.30	+41 29 46.8	4615	41	Ab
02 54 56.31	+42 53 33.7	19512	28	Ab
02 54 57.02	+41 07 31.9	37226	49	Ab
02 54 59.86	+42 11 06.0	51347	38	Ab
02 54 59.90	+41 36 56.1	4990	68	Em
02 55 00.36	+41 48 22.4	45742	45	Ab
02 55 00.60	+41 19 53.3	19842	60	Em
02 55 00.60	+42 08 32.0	5613	26	Ab
02 55 01.80	+41 26 51.3	4918	51	Ab
02 55 02.00	+41 31 30.4	5781	22	Ab
02 55 02.13	+41 03 49.5	4556	41	Ab
02 55 02.40	+41 36 24.1	4175	18	Ab
02 55 04.80	+42 15 45.8	5223	23	Ab
02 55 05.53	+41 38 28.9	5377	32	Ab
02 55 06.00	+41 44 00.4	5926	53	Ab
02 55 08.20	+41 29 17.1	4917	40	Ab
02 55 09.88	+42 48 07.4	9327	67	Em
02 55 14.10	+41 24 30.7	19663	32	Em
02 55 14.10	+41 47 29.8	5797	52	Ab
02 55 14.56	+41 41 53.4	18497	25	Ab
02 55 16.60	+41 20 20.5	5324	31	Ab
02 55 16.81	+42 01 59.6	69098	58	Ab
02 55 17.33	+41 34 49.0	5177	24	Ab
02 55 18.67	+41 44 06.2	49876	60	Ab
02 55 19.01	+41 34 28.0	5411	21	Ab
02 55 19.80	+40 43 54.9	83	64	star
02 55 20.97	+41 38 33.9	4742	38	Ab
02 55 23.70	+41 36 12.8	18501	37	Ab
02 55 25.06	+41 38 00.2	18457	36	Ab
02 55 26.38	+41 04 45.5	51196	59	Ab
02 55 27.10	+41 48 22.7	14	50	star
02 55 27.45	+41 20 24.1	62316	103	Ab
02 55 28.58	+41 44 41.0	5685	18	Ab
02 55 28.91	+42 02 33.3	36981	44	Ab
02 55 32.50	+41 29 53.3	5735	49	Ab
02 55 33.72	+41 35 37.0	51213	76	Ab
02 55 35.06	+41 53 33.5	51539	39	Ab
02 55 36.24	+43 03 29.7	6268	19	Em
02 55 36.74	+41 51 33.5	31897	460	Ab
02 55 37.50	+42 02 05.6	37082	31	Em
02 55 37.70	+41 47 07.4	18749	54	Em
02 55 38.48	+41 27 58.4	5600	63	Ab
02 55 38.61	+41 20 30.4	18284	89	Em
02 55 39.15	+41 42 24.1	51553	28	Ab
02 55 40.27	+41 01 51.5	19631	45	Ab
02 55 41.14	+41 48 39.9	51262	45	Ab
02 55 41.21	+42 02 11.1	50798	71	Ab

TABLE 1—*Continued*

α_{2000}	δ_{2000}	cz (km s^{-1})	σ_{cz} (km s^{-1})	Spectral Type
02 55 43.55	+41 28 37.7	5538	66	Ab
02 55 44.03	+41 07 48.0	5559	17	Ab
02 55 44.13	+41 36 51.3	14355	14	Ab
02 55 45.41	+43 15 16.3	8	22	star
02 55 47.43	+41 15 39.9	56471	72	Em
02 55 47.67	+41 56 12.3	76	48	star
02 55 48.00	+41 59 20.1	4423	23	Ab
02 55 48.77	+42 32 47.6	17932	21	Em
02 55 49.90	+41 56 52.4	4385	70	Em
02 55 49.95	+42 09 42.5	46317	77	Ab
02 55 51.80	+41 32 39.0	4224	77	Ab
02 55 52.63	+42 01 14.4	18715	43	Ab
02 55 52.80	+40 49 05.6	5727	31	Ab
02 55 53.04	+41 32 36.3	18051	71	Em
02 55 53.41	+41 24 41.7	51032	47	Ab
02 55 54.00	+41 44 37.6	4317	94	Ab
02 55 55.30	+41 34 58.1	4748	27	Ab
02 55 56.33	+41 13 23.2	18963	108	Ab
02 55 58.18	+41 20 20.1	51029	52	Ab
02 55 58.70	+42 01 03.2	104	31	star
02 55 58.97	+41 03 20.1	19599	22	Ab
02 55 59.20	+41 36 10.4	5957	67	Ab
02 55 59.69	+41 17 06.0	50973	40	Ab
02 56 01.43	+40 59 56.0	57226	40	Ab
02 56 04.61	+41 38 08.7	4466	29	Ab
02 56 05.76	+39 59 38.8	8964	66	Em
02 56 06.29	+41 05 14.3	19563	45	Ab
02 56 07.40	+41 37 51.1	5948	26	Ab
02 56 08.90	+42 00 24.3	50871	55	Ab
02 56 14.40	+42 09 10.6	46092	70	Ab
02 56 14.82	+41 38 50.8	5234	59	Ab
02 56 14.86	+41 03 20.0	50899	79	Ab
02 56 15.51	+41 52 40.8	15880	68	Em
02 56 16.52	+41 15 40.9	20033	28	Ab
02 56 22.47	+41 54 34.8	32392	26	Ab
02 56 23.69	+41 02 55.6	16493	66	Em
02 56 24.38	+41 33 47.5	39974	93	Ab
02 56 26.70	+41 07 59.1	5092	41	Ab
02 56 30.10	+42 16 35.9	5882	53	Ab
02 56 30.82	+41 35 54.4	18792	46	Ab
02 56 32.60	+41 00 44.3	5596	18	Ab
02 56 32.93	+41 52 01.9	15876	66	Em
02 56 33.46	+41 07 13.8	51355	77	Em
02 56 36.48	+43 02 50.3	2372	25	Ab
02 56 36.51	+41 30 32.1	50290	62	Ab
02 56 37.40	+41 47 23.5	18766	56	Em
02 56 37.70	+41 34 58.7	18585	26	Ab
02 56 37.77	+41 40 38.0	58504	63	Ab
02 56 38.24	+41 45 54.2	8715	65	Em
02 56 38.43	+41 13 05.6	16574	38	Em
02 56 38.60	+41 19 59.8	4633	10	Ab
02 56 39.21	+41 06 41.4	19470	42	Ab
02 56 42.25	+41 42 41.4	18499	30	Ab
02 56 42.43	+41 36 15.3	18582	82	Ab
02 56 43.03	+41 13 24.3	18617	23	Ab
02 56 44.10	+41 52 49.9	14422	65	Em
02 56 44.84	+41 41 03.5	18498	33	Ab
02 56 45.10	+41 35 04.9	18747	23	Ab
02 56 45.92	+41 46 36.2	18272	32	Ab
02 56 46.12	+41 46 28.8	18465	39	Em
02 56 48.92	+41 46 00.3	18968	44	Ab
02 56 50.26	+41 26 53.8	5206	82	Em
02 56 50.35	+41 31 01.6	18931	26	Ab
02 56 51.41	+41 15 47.8	88324	55	Ab
02 56 53.87	+41 56 57.6	62482	97	Ab
02 56 53.90	+41 39 33.2	5374	45	Ab

TABLE 1—*Continued*

α_{2000}	δ_{2000}	cz (km s^{-1})	σ_{cz} (km s^{-1})	Spectral Type
02 56 54.26	+40 59 32.4	16341	65	Em
02 56 54.39	+41 40 42.2	18664	26	Ab
02 56 54.63	+41 27 36.7	51002	58	Ab
02 56 54.72	+41 23 43.3	5594	60	Ab
02 56 55.08	+41 34 12.7	18678	42	Ab
02 56 56.03	+41 20 49.5	5153	40	Ab
02 56 56.20	+41 58 41.9	5331	16	Ab
02 56 56.40	+40 48 14.4	14424	66	Em
02 56 57.87	+41 51 29.7	18812	20	Ab
02 57 06.31	+41 53 59.0	16788	20	Em
02 57 08.46	+42 11 22.7	18937	16	Em
02 57 08.97	+41 31 00.2	6334	30	Ab
02 57 09.20	+40 59 59.7	37421	45	Ab
02 57 09.85	+41 03 39.4	5022	66	Em
02 57 15.70	+41 22 50.4	39	34	star
02 57 17.88	+41 21 10.5	37523	67	Em
02 57 19.20	+41 43 33.3	18789	53	Em
02 57 22.00	+41 56 19.5	4439	20	Ab
02 57 24.61	+41 43 57.0	50869	60	Ab
02 57 24.65	+41 25 57.4	16165	67	Em
02 57 27.12	+41 42 27.2	10758	65	Em
02 57 30.02	+41 21 13.7	51431	60	Ab
02 57 30.95	+41 37 56.6	50194	40	Ab
02 57 30.97	+41 37 49.3	4498	42	Ab
02 57 32.17	+41 39 39.9	50407	49	Ab
02 57 33.50	+41 30 57.9	4943	21	Ab
02 57 34.11	+41 43 38.5	50311	38	Ab
02 57 36.79	+41 32 56.9	5121	22	Ab
02 57 36.87	+42 00 47.7	19284	41	Em
02 57 36.92	+41 45 23.8	19258	53	Ab
02 57 36.98	+41 08 03.3	16551	65	Em
02 57 37.26	+41 33 27.6	51404	60	Ab
02 57 37.50	+42 00 31.7	31976	41	Em
02 57 37.83	+41 36 58.2	49773	78	Ab
02 57 38.84	+41 36 20.7	49773	68	Em
02 57 39.17	+41 33 12.3	51227	35	Ab
02 57 40.91	+41 45 31.0	50381	57	Ab
02 57 41.30	+41 14 21.1	50703	47	Ab
02 57 41.56	+41 56 26.5	11585	17	Ab
02 57 42.00	+41 04 21.8	69780	47	Ab
02 57 42.40	+41 32 51.5	51406	102	Ab
02 57 42.62	+43 12 26.0	15532	35	Ab
02 57 42.66	+41 12 38.8	37417	43	Ab
02 57 46.49	+41 55 22.2	19262	15	Em
02 57 47.57	+41 56 21.2	24168	24	Ab
02 57 48.02	+41 01 53.0	37565	65	Ab
02 57 57.22	+42 46 05.9	5338	35	Ab
02 58 11.85	+42 55 28.0	5417	44	Ab
02 58 12.40	+41 42 11.9	5658	26	Ab
02 58 17.60	+42 06 59.8	16253	27	Ab
02 58 21.90	+41 57 12.6	18762	72	Em
02 58 31.50	+40 51 39.1	9048	38	Ab
02 58 37.60	+40 52 06.4	9088	28	Ab
02 58 49.80	+41 57 12.6	18536	45	Ab
02 58 54.10	+40 44 57.7	9038	15	Em
02 58 58.80	+41 17 17.5	5065	25	Ab
02 59 00.52	+42 47 29.3	17063	67	Em
02 59 01.10	+42 20 45.5	4954	22	Ab
02 59 15.30	+42 21 54.1	19054	42	Em
02 59 17.23	+42 54 13.7	8508	20	Em
02 59 19.30	+42 01 13.9	16536	68	Em
02 59 32.20	+41 22 32.8	5753	20	Ab
02 59 41.10	+41 34 54.8	4956	28	Ab
02 59 53.36	+41 32 43.8	5625	23	Ab
03 00 00.77	+42 14 40.0	10252	20	Em
03 00 10.57	+42 58 17.1	17588	21	Em

TABLE 1—*Continued*

α_{2000}	δ_{2000}	cz (km s^{-1})	σ_{cz} (km s^{-1})	Spectral Type
03 00 37.50	+40 15 05.1	1931	67	Em
03 00 39.77	+40 52 45.0	5522	67	Em
03 00 40.99	+42 22 06.6	6013	25	Ab
03 00 54.87	+41 42 21.0	4911	32	Ab
03 00 58.05	+43 00 49.9	5025	25	Ab
03 00 59.45	+43 01 03.5	4828	22	Ab
03 01 01.77	+41 21 32.2	18819	31	Ab
03 01 02.19	+41 22 03.7	18934	30	Ab
03 01 09.95	+41 23 47.5	3738	66	Em
03 01 12.67	+41 43 02.8	5741	25	Em
03 01 25.79	+42 52 20.4	23676	29	Ab
03 01 34.68	+41 29 14.8	18374	31	Ab
03 01 48.66	+42 55 57.2	5152	66	Em
03 01 49.86	+42 38 31.2	4266	15	Em
03 01 50.00	+41 28 10.4	18569	36	Ab
03 01 59.78	+40 45 25.6	16086	16	Em
03 01 59.86	+42 35 05.8	4246	68	Em
03 02 01.88	+42 10 23.9	18449	27	Em
03 02 06.73	+41 35 36.6	9135	32	Ab
03 02 19.90	+40 54 00.3	4703	98	Ab
03 02 20.07	+41 59 05.4	6736	25	Ab
03 02 31.26	+42 12 53.8	30	28	star
03 02 35.14	+41 47 54.2	18786	46	Ab
03 02 38.69	+42 06 02.0	18905	68	Em
03 02 44.32	+41 37 30.6	4976	30	Ab
03 02 49.28	+40 58 16.0	4851	54	Ab
03 03 04.69	+40 58 40.6	15988	31	Em
03 03 12.83	+40 48 36.6	−24	27	star
03 03 30.86	+41 36 23.3	4797	28	Ab
03 03 36.80	+41 09 56.8	4871	21	Ab
03 03 37.36	+41 03 36.9	15883	67	Em
03 03 46.65	+42 15 44.0	19149	29	Ab

NOTE.—Units of right ascension are hours, minutes, and seconds, and units of declination are degrees, arcminutes, and arcseconds. α and δ (J2000), redshift, error in redshift, and spectral type (Ab/Em) for all targets with measured redshifts. Some objects are stars; these are flagged in the fifth column.

the same object observed under different configurations. Only 22 of these are cluster members. The Hydra targets are all within the central $1.^{\circ}4 \times 1.^{\circ}4$ of the cluster.

The magnitude completeness of the Hydra sample is complicated. Not only were we unable to measure a redshift for every target, but the original target list itself did not include every galaxy (up to some limit) in a magnitude-ordered list because of physical constraints in allocating fibers to objects. Moreover, the initial magnitude ranking was not by total galaxy luminosity but rather by luminosity within the central 3″ subtended by the fibers. We will discuss the photometry and luminosity function of AWM 7 in a later paper; here, we are interested primarily in the kinematics of the cluster and the incompleteness is not a limitation on the analysis.

3. DATA REDUCTION

We reduced all spectra using the XCSAO task of the RVSAO package in IRAF (Kurtz & Mink 1998). XCSAO measures redshifts by cross-correlating the observed spectra against a suite of template spectra. The quality of the match is measured by the parameter R, an estimate of the ratio of the highest peak to the average noise peak in the correlation function. The template spectra are themselves empirically derived from an archive of FAST observations and are thus strictly speaking directly applicable only to other FAST spectra. For the FAST velocities, the instrumental velocity offset with respect to the night sky lines is less than 10 km s^{-1} and is indistinguishable from zero (Kurtz & Mink 1998). We have found that the FAST template spectra are reliable also for the MMT and Hydra spectra; for those objects observed with several spectrographs, the redshifts derived from the separate spectra all agree to within the errors.

Many of the Hydra spectra have very low signal-to-noise ratios. We assess the robustness of the redshifts as follows: for each object, we construct all $2^N - 1$ possible (nonzero) combinations of spectra from the N individual exposures. N is 4 or 5 for most objects, and 8, 9, or 10 for objects observed in two configurations. For the few objects observed in three configurations, with N as large as 13, we examine only a subset of the 8191 possible combinations. We measure the redshift independently from each of these combined spectra. We accept a redshift for a target only if the following criteria all hold: (1) the R value increases with the number of individual spectra contained in the combined spectrum; (2) the velocity of the combined spectra stabilizes as the number of constituent individual spectra increases; and (3) the best combined spectrum has an R value >3.

The comparatively narrow spectral range of the Hydra observations means that Hα is shifted off the edge of the detector for $cz \gtrsim 20{,}000$ km s^{-1}. Cross-correlating emission line galaxies at these redshifts with the standard emission-line template results in a spurious redshift because the strongest remaining line in the spectrum is usually fit to Hα. We solved this problem by constructing a new template that differs from the standard emission-line template only by the absence of the Hα-nitrogen complex and the $\lambda\lambda$6717, 6731 sulfur lines.

We add an extra term of 65 km s^{-1} in quadrature to the errors of velocities determined from emission-line templates because the line-emitting region may be offset in velocity from the systemic velocity of the galaxy (Kurtz & Mink 1998).

Emission-line galaxies preferentially yield redshifts because an emission-line galaxy can be robustly matched to an emission template even when the signal-to-noise ratio in the continuum is too low for a believable correlation with an absorption template. Thus, the completeness limit for emission-line galaxies is effectively fainter than for galaxies with no emission. The Hydra configuration observed through cirrus yielded few redshifts, resulting in a brighter effective magnitude limit; this effect is minor because there is considerable overlap on the sky among the four configurations.

3.1. *Spectral Classification*

We divide our spectra into two broad classes, emission (Em) and absorption (Ab), based on the presence or absence of Hα in the spectrum. Hα is "present" if its equivalent width exceeds 5 Å. The robustness of this criterion is clearly a function of the signal-to-noise ratio of the spectrum; galaxies with low signal or with intrinsically weak Hα emission may be misclassified as absorption-line galaxies if the Hα peak does not rise appreciably above the noise. The misclassification is all in one direction: although some emission line galaxies may be misclassified as absorption, no absorption-line galaxy will be mistakenly classified as having emission.

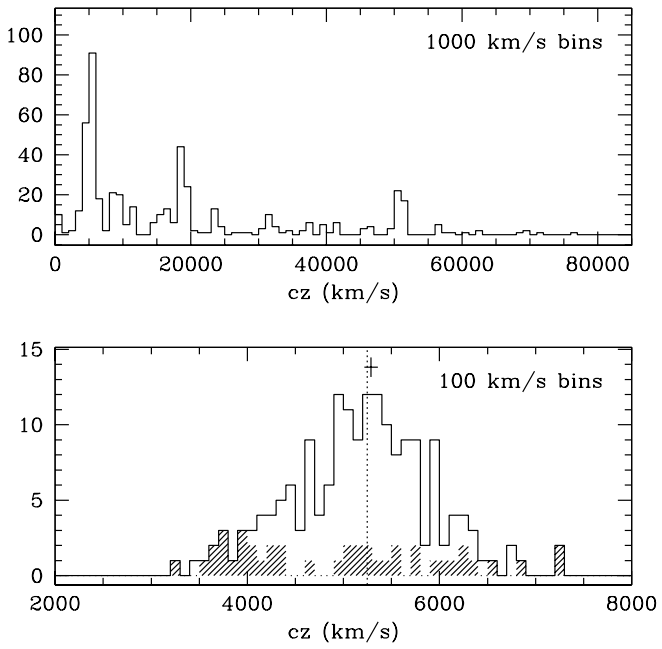

FIG. 1.—*Upper panel:* Velocity histogram of all observed targets. *Lower panel:* Velocity histogram of cluster members. The solid histogram denotes the entire sample (both Em and Ab galaxies); the hatched histogram denotes Em galaxies only. The dotted vertical rule indicates the mean redshift of the Ab galaxies; the solid vertical dash over the histogram indicates the redshift (and error) of the central cD galaxy.

4. THE DATA

Figure 1 (*upper panel*) shows the velocity distribution of all the observed galaxies. The cluster AWM 7, defined as in Koranyi et al. (1998) to consist of galaxies with redshifts in the range 2500–7500 km s^{-1}, is cleanly and unambiguously distinguished from the background. The lower panel shows the velocity histogram of the cluster galaxies only; the solid histogram indicates the distribution of the entire sample, and the hatched histogram indicates the Em galaxies alone. Our cluster sample consists of 179 galaxies; we classify 42 as Em and 137 as Ab. A Kolmogorov-Smirnov test indicates that the probability of the Em and Ab samples being so discrepant if drawn from the same distribution is small ($P_{D>D_{obs}} = 0.0004$); we conclude that the underlying distributions are different at the $\sim 4\,\sigma$ confidence level.

We compute the mean velocity and dispersion for the different galaxy populations following the prescription of Danese, De Zotti, & di Tullio (1980); the results are in Table 2. The Em galaxies have a much larger dispersion ($\sim$1100 km s^{-1} vs. $\sim$600 km s^{-1}) and are systematically offset in redshift by $\sim$400 km s^{-1} from the Ab population (4800 km s^{-1} vs. 5200 km s^{-1}). The extrema of the Em galaxies' velocity histogram are almost equidistant from the Ab mean velocity, but near 3800 km s^{-1} there is an excess of Em galaxies above the otherwise almost uniform distribution; this excess decreases the mean redshift. Neither the 17 Em galaxies with 3500 km s^{-1} $< cz <$ 4500 km s^{-1} nor the 12 with 3700 km s^{-1} $< cz <$ 4300 km s^{-1} evince any strong clustering on the sky. Absent independent distance measurements to these galaxies, it is difficult to determine whether they are foreground interlopers or whether the cluster Em galaxy population is indeed offset in velocity.

The cD galaxy near the cluster center, NGC 1129, has a redshift of 5288 $\pm$ 71 km s^{-1}, which, within the errors, is at rest with respect to the absorption-line galaxy population. The peak of the *ROSAT* PSPC hard X-ray emission map, defined as the center of the pixel containing the greatest flux, is 6″ from the nominal position of NGC 1129. We therefore adopt its position, $(\alpha, \delta)_{J2000} = (02^h54^m27^s.50, +41°34'42''.50)$, as the center of the cluster.

Figure 2 shows the distribution of galaxies with measured redshifts on the sky. Open circles and filled triangles denote Ab and Em galaxies in the cluster, respectively; crosses denote foreground or background galaxies. We do not plot targets for which we were unable to measure a redshift. The enhancement in the surface number density near the center of the cluster is due to the fainter magnitude limit reached by the MMT and Hydra observations; most Hydra targets turned out to be background sources.

The Em galaxies are distributed much more uniformly on the sky than the Ab galaxies; the projected surface density of the Ab galaxies increases strongly toward the center, but the Em galaxies show no such enhancement. A two-dimensional Kolmogorov-Smirnov test (Press et al. 1992) indicates that the probability of drawing two such discrepant samples from the same underlying distribution is less than 5×10^{-5}. The distribution of Ab galaxies is strongly flattened; there is a pronounced elongation in the east-west direction.

The X-ray emission from AWM 7 is similarly elongated; Mohr et al. (1995) compute an axial ratio of 0.665 $\pm$ 0.089 at a position angle of $-83° \pm 7°$ from the X-ray flux within 7′.5 of the cluster center, in perfect agreement with the value of 0.67 computed by Dell'Antonio, Geller, & Fabricant (1995) for an isothermal ellipsoid model density distribution. Mohr et al. (1995) report X-ray ellipticities for 58 clusters; AWM 7 is more flattened than both the mean and median clusters, but there are 10 clusters that are more flattened still. In our case it is difficult to measure the flattening quantitatively from our optical sample for comparison with the X-ray results because the completeness limit varies across our survey.

TABLE 2

VELOCITY DISTRIBUTION

Sample	N_{gal}	$\overline{cz}$ (km s^{-1})	$\sigma_{\overline{cz}}$ (km s^{-1})	σ_p (km s^{-1})	σ_{200} (km s^{-1})
Em + Ab.....	179	5186.2	54.3	$727.0^{+41.9}_{-35.8}$	...
Em.....	42	4821.5	168.0	$1088.8^{+143.4}_{-103.0}$	...
Ab_{137}.....	137	5247.6	49.0	$573.7^{+38.3}_{-32.0}$	$601.5^{+46.1}_{-37.6}$
Ab_{135}.....	135	5256.6	46.7	$542.9^{+36.6}_{-30.5}$	$578.1^{+44.5}_{-36.3}$

NOTE.—Velocity dispersions are computed from galaxies within 1.72 h^{-1} Mpc of the cluster center for Ab samples, and within 1.80 h^{-1} Mpc for Em and Em+Ab samples. σ_{200} is the projected velocity dispersion within r_{200} (§ 5.1).

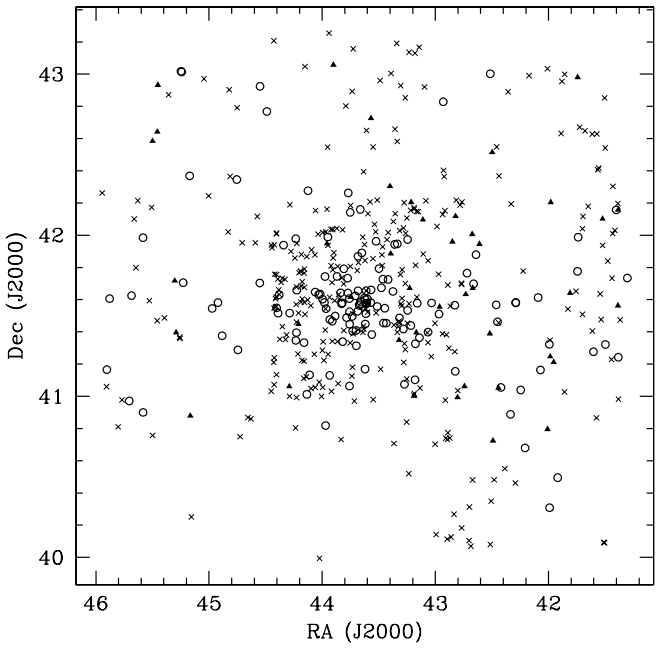

FIG. 2.—Position on the sky of all objects with measured redshifts. Note the denser sampling at the center, in the region covered by the Hydra and MMT observations. Crosses denote foreground and background objects. Open circles denote Ab galaxies in the cluster. Filled triangles denote Em galaxies in the cluster. Coordinate axes are in decimal degrees.

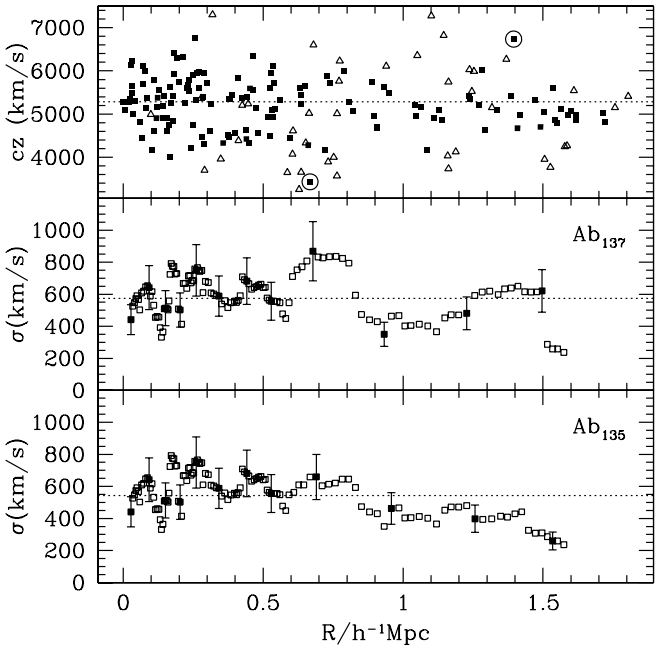

FIG. 3.—*Top panel:* Velocity as a function of projected distance from the cluster center. Ab galaxies are filled squares, Em galaxies are open triangles. The two outliers are circled. *Middle panel:* Velocity dispersion profile for the 137 Ab galaxies in the cluster sample. Every 11th point is independent and is shown with 1 σ error bars. The horizontal rule indicates these galaxies' overall dispersion of 574 km s^{-1}. *Bottom panel:* Same as middle panel, but with two outliers removed. Horizontal rule is now at 543 km s^{-1}.

Redshifts of cluster galaxies plotted against distance from the cluster center define a trumpet-shaped locus delimited by caustics (Kaiser 1987). Galaxies inside the caustics are bound to the cluster; those outside are unbound. We construct such a plot in Figure 3 (*top panel*); again, squares are Ab galaxies and triangles are Em galaxies. Although one can discern by eye where the caustics probably lie, they are in practice poorly defined. Their accurate determination requires many more galaxies than our sample contains (Diaferio 1999; Diaferio & Geller 1997; Geller et al. 1999).

From the velocity histograms and the position-velocity diagrams, it is clear that the Em and Ab galaxies are not equivalent tracers of the cluster mass. A friends-of-friends algorithm (Huchra & Geller 1982) for finding substructure suggests that many of the Em galaxies are contained in smaller subgroups distinct from the main cluster (*not shown*); these may be accreting onto the cluster now and, not yet being virialized, do not follow the dark matter distribution as closely as the Ab galaxies. There is considerable radial segregation of Ab and Em galaxies; the radial distribution of Em galaxies is more uniform and has a greater mean and median distance from the cluster center than that of the Ab galaxies. This behavior is observed in other clusters (Mohr et al. 1996; Adami, Biviano, & Mazure 1998), in groups (Mahdavi et al. 1999), and in the field as the morphology-density relation (Dressler 1980). Moreover, the velocity dispersion of the Em galaxies remains large with increasing radius while that of the Ab galaxies declines (see § 5). These considerations suggest that the Em galaxies are not virialized tracers of the underlying dark matter distribution. Because our goal is an accurate determination of the mass profile, we exclude the Em galaxies from further analysis, following Mohr et al. (1996). We will revisit the issue of substructure in and around AWM 7 and other poor clusters in a subsequent paper.

Figure 3 (*middle panel*) shows the velocity dispersion profile constructed only from the Ab galaxies. We sort the galaxies by distance from the cluster center, then evaluate the velocity dispersion in a sliding bin containing 11 galaxies; we plot the dispersion as a function of the mean distance to the galaxies in the bin. Neighboring points are strongly correlated, as they share 10 of their 11 galaxies; every 11th point (*distinguished by error bars*) is independent.

Two large excursions from the overall trend dominate the profile. Two outlier galaxies, one at projected distance $R \sim 0.7\ h^{-1}$ Mpc and low velocity, the other at $R \sim 1.4\ h^{-1}$ Mpc and high velocity (*circled* in the *top panel* of the figure) produce these excursions. It is clear that these two galaxies are responsible because the number of data points in each excursion equals the width of the sliding bin used to compute the profile. We therefore define a subset of the Ab sample, Ab_{135}, excluding these two galaxies. We shall henceforth refer to the entire sample of 137 Ab galaxies as Ab_{137}. The velocity dispersion profile for Ab_{135} appears in the lower panel; the overall dispersion of these 135 galaxies is 543^{+37}_{-31} km s^{-1} within $R = 1.7\ h^{-1}$ Mpc. After some fluctuations near the core, the profile becomes smooth and shows the characteristic declining profile seen in poor groups by Mahdavi et al. (1999) and in some N-body simulations (e.g., Crone, Evrard, & Richstone 1994). The decline in dispersion at small radii matches that of the "type C" clusters of Girardi et al. (1998). We revisit the issue of the cold core in § 6.

5. MASS PROFILE

We compute the mass profile of AWM 7 in two largely independent ways. First, we assume that the mass profile follows the functional form predicted by the hierarchical

clustering simulations of Navarro et al. (1995, 1996, 1997). This model has two parameters, which we derive separately from the observations under the assumption that the Ab galaxies are virialized and that they trace the dark matter distribution. While this is a restrictive assumption, there is growing evidence that the NFW profile is applicable beyond the hierarchical clustering regime in which it was proposed. Huss, Jain, & Steinmetz (1999) find from high-resolution N-body simulations that virialized dark matter halos with different formation histories nevertheless evince similar density and velocity dispersion profiles, and that this "universal" density profile is well described by the functional form of the NFW model. The collapse history of the cluster seems immaterial in determining the ultimate cluster profile. More concretely, Geller et al. (1999) show that this profile describes the Coma cluster well for $R \lesssim 10\ h^{-1}$ Mpc. For comparison, we also fit a nonsingular isothermal sphere to AWM 7.

We also compute the mass profile from the virial theorem alone. At small radii, this method gives incorrect results if not corrected for the exclusion of the outer cluster regions from the computation. The mass profile can be corrected with a surface term, which depends on both the mass and velocity dispersion profiles. These last two profiles are linked to the velocity anisotropy profile through the Jeans equation (e.g., Binney & Tremaine 1987), but the data are insufficient to constrain the problem completely. Usually one makes some assumptions about one or more of the profiles and solves for the others (e.g., Binney & Mamon 1982; The & White 1986; Binney & Tremaine 1987; Girardi et al. 1998). Here, we make these assumptions only for the computation of the surface term correction to the virial mass estimator.

5.1. *The NFW model*

5.1.1. *Description*

The spherically symmetric NFW density distribution is

$$\rho(r) = \frac{\delta_c \rho_c}{(r/r_c)(1 + r/r_c)^2}\,, \tag{1}$$

resulting in the enclosed mass profile

$$M(<r) = 4\pi\delta_c \rho_c r_c^3 \left[\log\left(1 + \frac{r}{r_c}\right) - \frac{r/r_c}{1 + r/r_c}\right], \tag{2}$$

where ρ_c is the critical density of the universe and δ_c and r_c are the two parameters of the model, corresponding to the overall normalization and the core radius, respectively. The radial scale in the context of cluster simulations is often quoted in units of r_{200}, the radius where the mean cluster density has dropped to $200\rho_c$. NFW claim, on the basis of numerical experiments, that this radius approximately separates the virialized and infall regions (see also Cole & Lacey 1996). NFW define the "concentration parameter" $c = r_{200}/r_c$. A low value of c arises if the core radius is comparable with the overall extent of the cluster, that is, if the mass profile is not very concentrated toward the center. NFW demonstrate that more massive clusters are less concentrated, with the concentration parameter related to the overall normalization by

$$\delta_c = \frac{200}{3}\,\frac{c^3}{\log(1 + c) - c/(1 + c)}\,. \tag{3}$$

Because the enclosed mass of the NFW profile diverges logarithmically, it is customary to quote $M_{200} \equiv 200\rho_c(4\pi/3)r_{200}^3$ as the cluster mass.

5.1.2. *Fitting the NFW Model*

We can derive r_c observationally from the distribution of projected radii of cluster galaxies. The projected surface number density of galaxies in the NFW model is given by

$$\Sigma(\tilde{R}) \propto \frac{1 - X(\tilde{R})}{r_c^2(\tilde{R}^2 - 1)}\,, \tag{4}$$

where $\tilde{R} = R/r_c$ is the projected radius in units of the core radius, and

$$X(\tilde{R}) = \begin{cases} (1 - \tilde{R}^2)^{-1/2}\ \mathrm{sech}^{-1}\ \tilde{R}, & \text{if } \tilde{R} < 1\,, \\ (\tilde{R}^2 - 1)^{-1/2}\ \sec^{-1}\ \tilde{R}, & \text{if } \tilde{R} \geq 1\,. \end{cases} \tag{5}$$

Given the distribution of projected radii in our sample, we fit r_c with a maximum-likelihood technique by finding the value of r_c that maximizes the probability

$$\mathscr{L} = \prod_i \left[\frac{\tilde{R}_i\,\Sigma(\tilde{R}_i)}{\int_0^{\tilde{R}_{\max}(r_c)} \tilde{R}\Sigma(\tilde{R})\,d\tilde{R}}\right]^{w_i} \tag{6}$$

of observing that particular distribution of projected radii, where w_i is a weight assigned to each galaxy to account for the nonuniform magnitude limit of our survey. We assign each galaxy one of two possible weights as follows: galaxies within the central 0.51 h^{-1} Mpc of the survey, where it is 97% complete to $m_R = 17.2$, have $w = 1.00$; galaxies with $R_i > 0.51\ h^{-1}$ Mpc, where the survey is complete to $m_R = 15.5$, have $w = 1.95$, where 1.95 is the ratio of the number of galaxies with $m_R < 17.2$ to the number with $m_R < 15.5$ within 0.51 h^{-1} Mpc of the cluster center. This correction assumes that the luminosity function is the same in the core as in the outskirts of the cluster. We exclude galaxies fainter than $m_R = 17.2$ within 0.51 h^{-1} Mpc and fainter than $m_R = 15.5$ otherwise from the fit; there remain 53 galaxies with $R < 0.51\ h^{-1}$ Mpc and 70 with $R \geq 0.51\ h^{-1}$ Mpc. Both outliers remain in the sample. The denominator in equation (6) serves to normalize the intrinsic probability of observing a particular galaxy i at projected radius $\tilde{R}_i$ (expressed in the numerator) to the possible range of $\tilde{R}$ where it could be included in the sample. The upper limit of the integral is a function of r_c; $\tilde{R}_{\max}(r_c) = R_{\lim}/r_c$, where $R_{\lim}$ is the limiting projected radius of the survey. In practice, we use the largest projected radius in the sample for $R_{\lim}$. Table 3 lists the best-fit values of r_c for the Ab_{135} and Ab_{137} subsamples, computed from 121 and 123 galaxies, respectively, along with 1, 2, and 3 σ uncertainties, as determined by $\Delta(\log \mathscr{L}) = 0.5$, 1.0, and 1.5. There is little difference in the best-fit r_c for the two samples; if the Em galaxies are included, the best-fit r_c increases by $\sim 50\%$, because the Em

TABLE 3

NFW r_c FROM PROJECTED RADII

Sample	r_c (h^{-1} Mpc)	1 σ Range	2 σ Range	3 σ Range
Ab_{137}.....	0.223	0.174–0.285	0.157–0.316	0.145–0.342
Ab_{135}.....	0.211	0.164–0.270	0.148–0.299	0.137–0.324

NOTE.—r_c is computed from two-zone magnitude-limited samples of 123 and 121 members.

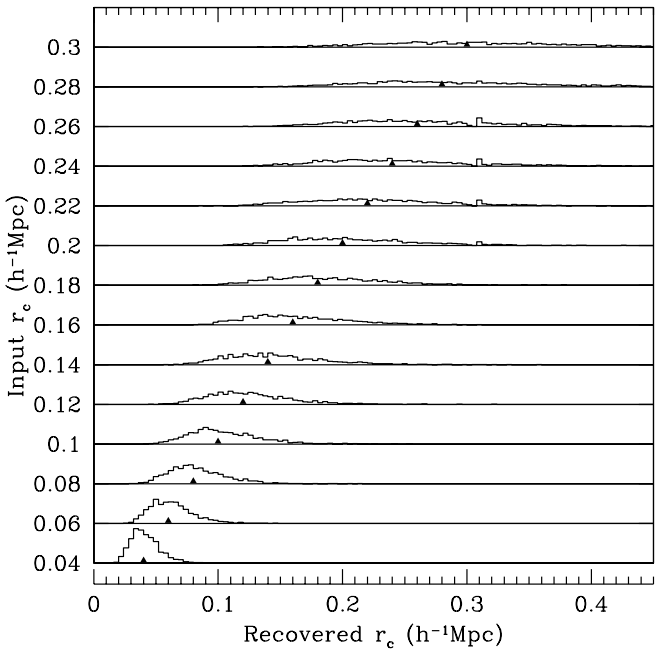

FIG. 4.—Histograms of recovered values of the NFW parameter r_c from 2000 Monte Carlo realizations of sets of 123 projected radii drawn from NFW models with varying r_c. The histograms are all to the same scale, but for the highest input r_c may extend off the right edge of the plot. The triangles in the histograms and the numbers along the vertical axis both indicate the input value of r_c.

galaxies are less centrally concentrated (Fig. 3). We compare the NFW model to the nonsingular isothermal sphere in § 5.2.

We use Monte Carlo simulations to assess the robustness of this method: for selected values of r_c, we construct 2000 sets of 123 projected radii drawn from the distribution of projected radii for an NFW profile with that r_c; we reproduce the nonuniform magnitude limit of our survey by accepting only galaxies with $R \geq 0.51\ h^{-1}$ Mpc with probability 1/1.95. We compute the maximum-likelihood recovered r_c using equation (6). Figure 4 shows the results for r_c in the range 0.04–0.30 h^{-1} Mpc. The median recovered r_c is within 0.002 of the input r_c in all but one case; however, the distributions of the recovered r_c are broad. The distribution of recovered r_c is narrowest for small r_c, and broadens as r_c increases, because (1) the peak in the probability distribution of projected radii becomes less pronounced as r_c increases, and because (2) we sample a smaller dynamic range of $\tilde{R}$ as r_c increases (because the limiting projected radius $R_{\rm lim}$ is constant). The distribution of the ratio of recovered to input r_c is largely independent of input r_c, however. The lower and upper 1 σ bounds (defined as the values of r_c enclosing 34.2% of the distribution on either side of the median) are typically displaced -25% and $+30\%$ from the true r_c, respectively. Increasing the sample size in the simulations to 500 radii (*not shown*) reduces the spread in the distribution of recovered r_c by a factor of ~ 2.

Knowing r_c, the NFW model would be completely specified if we also knew r_{200}, but this quantity is difficult to derive observationally. We can arrive at an estimate if we assume that the virial theorem holds, so that $M_v \equiv 3\sigma_p^2 r_v G^{-1}$, where G is the gravitational constant, r_v is the virial radius, and σ_p is the global line-of-sight cluster velocity dispersion. Then

$$\frac{M_{200} r_v}{M_v r_{200}^3} = 100\ H_0^2 \frac{(1+z)^3}{3\sigma_p^2}\,, \tag{7}$$

where he have used $\rho_c(z) = 3\ H_0^2(1+z)^3/(8\pi G)$ for $\Omega = 1$, and the definition of M_{200}. The right-hand side of this equation is observationally determined, and substituting for M_v and M_{200} using equation (2), the left-hand side becomes a function of r_c, r_v, and r_{200}, which we solve for r_{200}. We fit r_c from the distribution of projected radii and approximate r_v by

$$r_v \sim \frac{\pi}{2} \frac{N(N-1)}{\Sigma_i \Sigma_{i<j} R_{ij}^{-1}}\,, \tag{8}$$

where N is the number of galaxies in the system and R_{ij} is the projected separation between galaxies i and j (Binney & Tremaine 1987). This estimator yields $r_v \sim 1.30\ h^{-1}$ Mpc for the Ab_{137} sample and $r_v \sim 1.28\ h^{-1}$ Mpc for the Ab_{135} sample.

The value of r_{200} that solves equation (7) is fairly insensitive to the value of r_c; in the regime of interest, where 500 km s$^{-1} < \sigma_p < 600$ km s^{-1}, r_{200} varies $\sim 3\%$ as r_c ranges from 0.12 to 0.30 h^{-1} Mpc for any constant σ_p. The derived r_{200} is more sensitive to σ_p, varying $\sim 15\%$ over the range 500 km s$^{-1} < \sigma_p < 600$ km s^{-1} with constant r_c. For the r_v obtained from equation (8), the values of r_{200} are 1.02 and 0.97 h^{-1} Mpc for the Ab_{137} and Ab_{135} samples, respectively (Table 4). The corresponding value of the concentration parameter c, 4.6 in both cases, falls in the middle of the range 2.3–7.7 seen by Carlberg et al. (1997) for rich systems, although the errors are large in both cases. Comfortingly, the values are also smaller than the $c \sim 7.5$ that Mahdavi et al. (1999) find for their lower mass poor groups. For AWM 7, M_{200} is 2.47 and $2.13 \times 10^{14}\ h^{-1}\ M_\odot$ for the Ab_{137} and Ab_{135} samples, respectively. Here the larger mass is associated with a formally slightly smaller value of c (4.56 vs. 4.61), in keeping with the general trend seen by NFW, but this consistency may be accidental, considering the uncertainties in the computed values of c. It is interesting to note that two outliers (in a sample of 137) can alter the recovered mass by $\sim 15\%$.

Because the cluster extends beyond r_{200}, M_{200} in fact underestimates the total mass. Extrapolating the NFW

TABLE 4

NFW PROFILE PARAMETERS

Sample	r_c (h^{-1} Mpc)	r_{200} (h^{-1} Mpc)	c	δ_c	r_v (h^{-1} Mpc)	M_{200} ($10^{14}\ h^{-1}\ M_\odot$)	M ($<1.7\ h^{-1}$ Mpc) ($10^{14}\ h^{-1}\ M_\odot$)
Ab_{137}.....	0.223	1.02	4.6	7.1×10^3	1.30	2.47	3.49
Ab_{135}.....	0.211	0.97	4.6	7.2×10^3	1.28	2.13	3.01

NOTE.—r_c is computed from two-zone magnitude-limited samples of 123 and 121 members.

mass profile to 1.7 h^{-1} Mpc (the maximum radial extent of the Ab sample) with equation (2) yields 3.49 and 3.01 $\times$ 10^{14} h^{-1} $M_{\odot}$ for the Ab_{137} and Ab_{135} samples, respectively.

5.2. *Comparison to the Nonsingular Isothermal Sphere*

The nonsingular isothermal sphere (NSIS) arises from setting finite boundary conditions at zero radius to the same differential equation that gives rise to the singular isothermal sphere (e.g., Binney & Tremaine 1987, pp. 226–232). It is characterized by a density normalization ρ_0 and a core radius r_0 at which the projected density falls to 0.5013 of its central value. In Figure 5 we compare the fit of the projected surface number density from the NSIS and NFW models to the data. Although the maximum-likelihood technique of § 5.1.2 makes optimal use of the data, it provides no independent assessment of goodness of fit. Here, although with some loss of information, we bin the observed surface number density for comparison with the models; we retain the same weighting scheme as in the maximum-likelihood calculation.

The left panels of Figure 5 show the observed profile (*filled squares with Poisson error bars*), the NFW fit (*solid line*), and the NSIS fit (*dotted line*) for both the Ab_{135} (*upper panel*) and Ab_{137} (*lower panel*) samples. The right panels of the figure illustrate how the best-fit values of r_c, r_0, and χ^2/ν vary with the choice of binning; the profiles and fits are shown for 11 galaxy equivalents per bin (galaxies beyond 0.51 h^{-1} Mpc count as 1.95 equivalents).

For different binnings the quality of the fits of both the NFW and NSIS models, as measured by χ^2/ν, varies much less for the Ab_{135} sample than for the Ab_{137} sample. The best-fit values of r_c and r_0 are quite stable for both samples. The decreased sensitivity to the binning provides further justification for excluding the two outlier galaxies. For both samples, the NFW model fits with a lower χ^2/ν than the NSIS model, independent of the binning (except in one case). The superiority of the NFW model is more consistent for the Ab_{135} sample, although this superiority is not overwhelming; for Ab_{135}, NFW fits with $\chi^2/\nu = 1.075$, whereas the NSIS fits with $\chi^2/\nu = 1.233$. For Ab_{137}, the respective χ^2/ν for NFW and NSIS are 1.184 and 1.252 (all for 11 galaxies per bin). There is thus some formal statistical justification for using the NFW model over the NSIS, but an unambiguous determination would require a survey out to 2 or 3 h^{-1} Mpc (cf. Geller et al. 1999).

With 11 galaxies per bin, the best-fit values of r_c are within 5% of the maximum-likelihood values for both samples, and well within the 1 σ range for all binnings, indicating that the loss of information inherent in the binning is not severe.

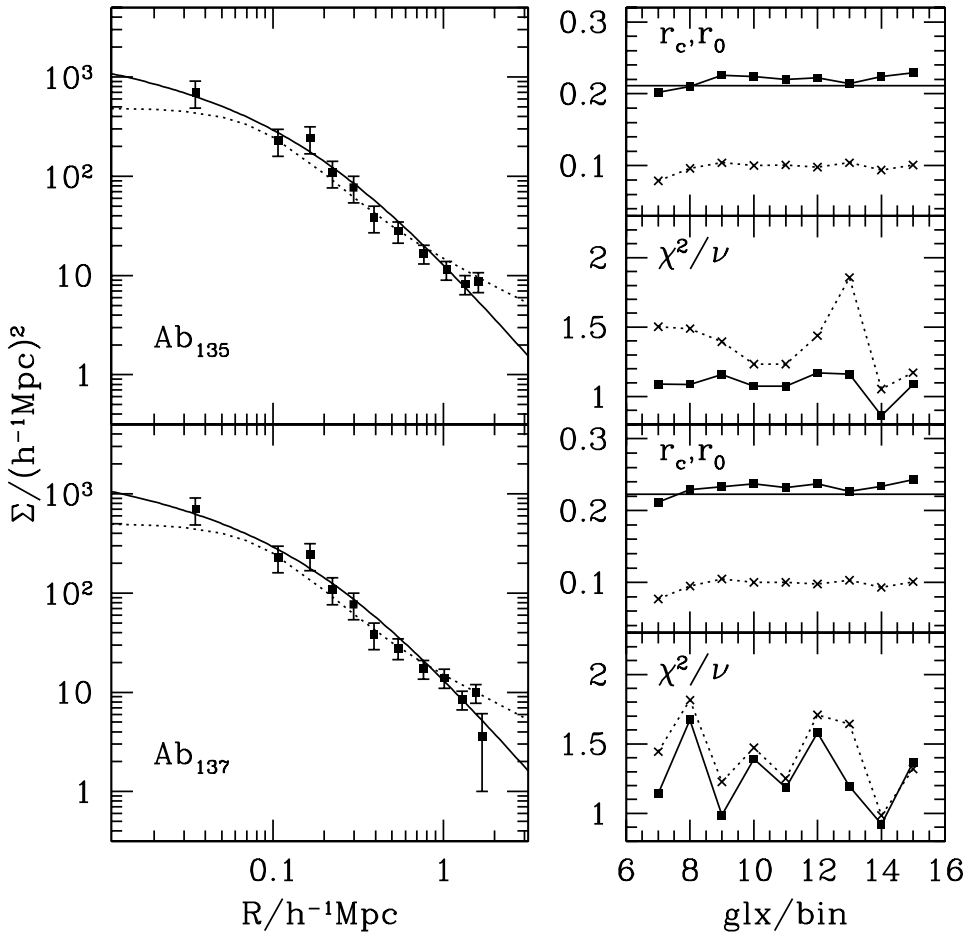

FIG. 5.—Comparison of the actual binned projected surface number density of galaxies to the NFW (*solid lines*) and nonsingular isothermal sphere models (NSIS; *dotted lines*). The upper panels refer to the Ab_{135} sample; the lower to the Ab_{137} sample. *Left panels:* Actual surface density profile (*filled squares with error bars*). There are 11 galaxies per bin. The lines show the best-fit NFW and NSIS models. *Right panels:* Dependence of the fits on the binning. The behavior of the best-fit value of r_c (for the NFW model) or r_0 (for NSIS) and of χ^2/ν is shown as a function of the binning. The horizontal rules indicate the maximum-likelihood values of r_c for the two samples.

5.3. *The Virial Mass Profile*

We now compute the mass profile of AWM 7 from the virial estimator appropriate for the case of galaxies embedded in a diffuse distribution of dark matter, under the added assumption that light traces mass. The appropriate estimator (Binney & Tremaine 1987) is

$$M_{\rm est} = \frac{3\pi N}{2G} \frac{\Sigma_i v_i^2}{\Sigma_i \Sigma_{j<i} |\boldsymbol{R}_i - \boldsymbol{R}_j|^{-1}} = \frac{3r_v}{G} \sqrt{\frac{\Sigma_i v_i^2}{N-1}}, \quad (9)$$

where v_i is the radial velocity relative to the cluster mean and $\boldsymbol{R}_i$ is the projected radius vector relative to the center of the cluster. This estimator assumes that the galaxies are in dynamical equilibrium within the cluster potential, that galaxies trace the dark matter distribution, and that the entire cluster has been observed. These assumptions do not apply to the Em galaxy population; indeed, when we apply this prescription to the Em galaxies alone, the resultant mass estimate is a factor of ~ 4 greater than for the Ab galaxies. To correct for the failure to include the entire angular extent of the cluster in our sample, we correct the mass estimate with a surface term $C(b)$ (The & White 1986) that depends on the limiting radius b of the observations. The corrected mass is

$$M_{cv}(<b) = M_{\rm est}[1 - C(b)]$$
$$= M_{\rm est}\left[1 - 4\pi b^3 \frac{\rho(b)}{\int_0^b 4\pi r^2 \rho(r)\, dr} \frac{\sigma_r^2(b)}{\sigma^2(<b)}\right], \quad (10)$$

where $\sigma(<b)$ denotes the integrated velocity dispersion within the limiting radius b (e.g., Girardi et al. 1998).

The surface term incorporates information about the velocity dispersion profile and the density profile; the former is measurable from the data, but some assumption must be made about the form of the density profile—in order to correct that very profile. The & White (1986) and Girardi et al. (1998) posit a functional form for the mass profile, which they then fit to the data on the basis of the projected number density of galaxies. Here we assume an underlying NFW mass profile.

5.3.1. *Behavior of the Surface Term*

The radial dependence in the NFW model of the surface term in equation (10) is

$$C_{\rm NFW}(r) = \frac{u^2}{(1+u)^2}\left[\log(1+u) - \frac{u}{1+u}\right]^{-1}\left[\frac{\sigma_r(r)}{\sigma(<r)}\right]^2, \quad (11)$$

where $u = r/r_c$. The last term involves both the overall velocity dispersion σ and the radial velocity dispersion σ_r and is thus a function of the anisotropy parameter $\beta = 1 - \sigma_\theta^2/\sigma_r^2$, which is itself a function of r. Now $\sigma^2 = \sigma_r^2 + \sigma_\theta^2 + \sigma_\phi^2$; under the assumption of spherical symmetry the last two terms are equal, so $\sigma_r^2 = \sigma^2/[3 - 2\beta(r)]$, which we substitute into the numerator of the last term for computation. The anisotropy and velocity dispersion profiles are not independent; they are coupled via the Jeans equation. Girardi et al. (1998) find that for their mass model a constant anisotropy profile $\beta(r) = 0$ produces a velocity dispersion profile that peaks at $\sim 0.1 r_v$, dips slightly in the core, and decreases gradually at large radii; the simple functional form $\beta(r) = -k/r$, where k is a constant, produces a velocity dispersion profile with a more severe dip in the core. In this case, the orbits in the core become purely tangential as $\beta \to -\infty$.

Figure 6 shows the behavior of the surface term for an NFW mass distribution and the observed velocity dispersion profile (Fig. 3) under the assumption of three different anisotropy profiles: constant (*top panel*), $\beta(r) = -k/r$ (*middle panel*), and $\beta(r) = 1 - k/r$ (*bottom panel*). The multiple curves in each panel correspond to the values of β (*top panel*) or k (*middle and bottom panels*) enclosed in brackets. One of the extreme curves is labeled in each case for reference. The values of k are chosen to bracket the value inferred from the profiles in Figure 3 of Girardi et al. (1998). Note that the three panels are not drawn to the same scale. Because these classes of β profile are derived from fits to the mass model of Girardi et al. (1998), they are not a priori strictly valid for the NFW profile; nevertheless, it is reasonable to adopt them here as representative of the general forms that the profiles may have.

By definition, the surface term must be everywhere less than unity (to ensure a positive mass). The results shown for constant large values of β are thus clearly unphysical. At small radii, the data are too noisy for all our assumptions to hold; a proper treatment would require a full solution of the Jeans equation. It is unlikely that this treatment would improve the results very much, however, because of the intrinsic noisiness and discreteness of the data. At larger radii, the variations in the surface term become less pronounced, and the surface term in general becomes less important, decreasing to $\lesssim 5\%$ for each profile at the outer limit of our sample. Sufficiently far from the core, then, the virial mass estimator provides a robust estimation of the

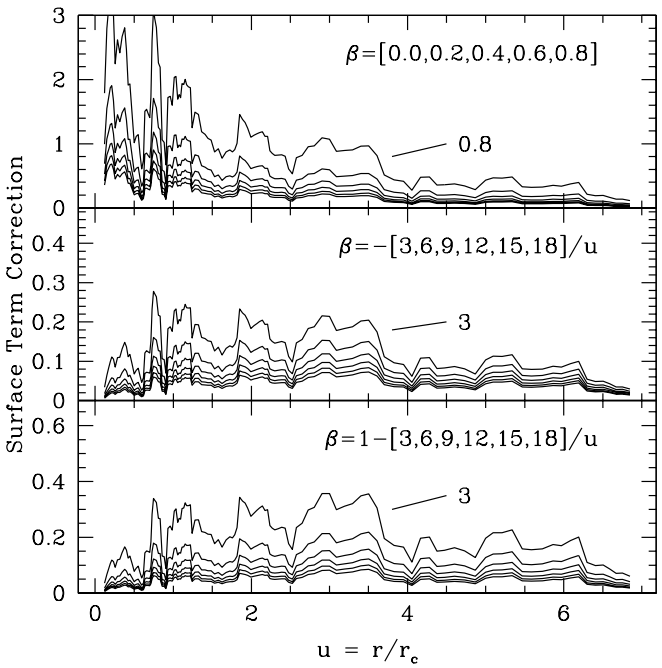

FIG. 6.—Behavior of the surface term correction to the virial mass estimator as given by eq. (10) assuming an underlying NFW mass profile for three models of the anisotropy profile $\beta(r)$. The assumed NFW profile uses $r_c = 0.211$ (the best-fit value for the $\rm Ab_{135}$ sample), and we use the observed velocity dispersion profile. *Top panel:* $\beta(r) = k$. *Middle panel:* $\beta(r) = -k/r$. *Bottom panel:* $\beta(r) = 1 - k/r$. k is a constant in each case. There is one line for each value of k listed in the label, with one of the extreme lines labeled for reference.

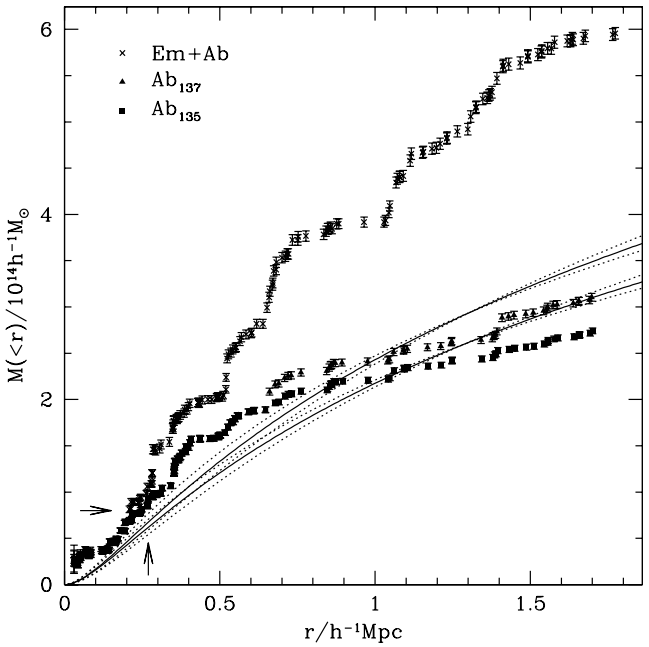

FIG. 7.—Enclosed mass profile as determined from the virial theorem, for Em, Ab_{137}, and Ab_{135} samples. Error bars show the formal bootstrap errors (see text). The solid lines are the independently derived NFW profiles tabulated in Table 4; the dotted lines are the profiles corresponding to the 1 σ ranges of r_c from Table 3 with r_{200} recomputed from eq. (7). The arrows point to the X-ray mass of Dell'Antonio et al. (1995).

enclosed cluster mass, but at small radii the surface correction is too variable to result in a reliable mass profile. The virial mass estimator thus seems to be a good tool for estimating total cluster masses, but it is not well suited to the determination of mass profiles in cluster cores, where the surface term correction is most important but least well determined.

A reliable description of the surface term at small radii may be possible only from cluster simulations in which the dark matter density and velocity distributions are fully known to the experimenter. In that case, empirical surface term profiles can be built from the data and compared to reconstructions that an observer would generate under various assumptions of the anisotropy profile.

5.3.2. *The Virial Mass Profile*

Figure 7 shows the virial mass profile (eq. [9]), with no surface term correction, as derived from three subsets of our galaxy sample: the entire sample (*crosses*), the Ab_{137} sample (*triangles*), and the Ab_{135} sample (*squares*). The entire (Em + Ab) sample is included only to illustrate that the inclusion of the emission-line galaxies with their larger velocity dispersion skews the results toward higher mass. Indeed, this difference is evident in the two Ab profiles as well: they agree up to the first outlier, at which point the Ab_{137} mass profile jumps; the two Ab profiles then grow more or less in parallel until the next outlier. We compute uncorrected enclosed masses within 1.7 h^{-1} Mpc of 3.10 and $2.74 \times 10^{14}\ h^{-1}\ M_\odot$ from the Ab_{137} and Ab_{135} samples, respectively. The surface term correction at this radius is on the order of 2%–5%, depending on the anisotropy.

TABLE 5

NFW AND VIRIAL MASSES

Sample	$M_{NFW}(<1.7\ h^{-1}$ Mpc) ($10^{14}\ h^{-1}\ M_\odot$)	$M_{VT}(<1.7\ h^{-1}$ Mpc) ($10^{14}\ h^{-1}\ M_\odot$)	$\Delta M/M_{VT}$
Ab_{137}.....	3.49	3.10	0.126
Ab_{135}.....	3.01	2.74	0.099

We estimate the error in the enclosed mass profile by the statistical bootstrap method (Diaconis & Efron 1983): for the N galaxies enclosed within a given projected radius, we compute the N possible enclosed masses from all subsets of $N-1$ galaxies. We take the standard deviation of the resultant set of masses as the formal error in the estimated enclosed mass. The formal errors become quite small, on the order of 3%, at large radii. When the number of galaxies is large and the distribution of velocities is well behaved, the random rearrangement of velocities has little effect on the mass estimate; thus, the distribution of the bootstrapped masses is narrow. The actual error is in fact larger, as demonstrated by the sensitivity to the outliers. The error in the enclosed virial mass is $\sim 15\%$.

The solid smooth curves indicate the NFW mass profiles we fitted previously, and the dotted lines indicate the profiles corresponding to the 1 σ ranges of r_c from Table 3 with r_{200} recomputed from equation (7). The agreement with the virial mass is quite good, to within $\sim 15\%$ at 1.7 h^{-1} Mpc for both Ab samples, with the virial mass the smaller of the two in each case. The agreement along the profile in general is reasonable given the uncertainty in the surface term. The discrepancy is greatest near $R \sim 0.5\ h^{-1}$ Mpc, corresponding to $r/r_c \sim 2$, where the surface term correction can be on the order of 20% in the proper direction; at the virial radius the masses are in perfect agreement, and at larger radii the NFW mass profiles overtake the virial mass profiles. Because r_{200} is insensitive to r_c, the variation in r_c results in little difference in the mass profile at large radii but of course has a greater effect on scales of a few times r_c. Table 5 compares the NFW and virial masses. Based on the sensitivity of the virial mass to the outliers and on the effect of the surface term, we assign an error of $0.5 \times 10^{14}\ h^{-1}\ M_\odot$ to our mass estimate.

Our mass profile is in agreement with the *ROSAT* X-ray mass of Dell'Antonio et al. (1995), who derive $M(<0.27) = 0.8 \times 10^{14}\ M_\odot$ (*arrows* in Fig. 7), and is within the allowable range of mass profiles determined from *ROSAT* data by Neumann & Böhringer (1995) and from *ASCA* data by Loewenstein & Mushotzky (1996) and Markevitch & Vikhlinin (1997). The X-ray masses are all quite uncertain and extend only to $R \sim 0.5\ h^{-1}$ Mpc. Koranyi et al. (1998) illustrate the range of mass profiles from X-ray determinations; the range is so broad as to include even the virial mass profile computed from emission-line galaxies; any plausible kinematic mass profile is thus likely to be consistent with the current X-ray limits on the mass. The increased sensitivity of the *Chandra Observatory* will allow X-ray mass profiles to be determined with more precision and to larger radii.

6. DISCUSSION

Galaxy clusters display a range of velocity dispersion profiles (e.g., den Hartog & Katgert 1996; Girardi et al. 1998). Some are peaked at the center, others are more or less flat, still others rise with increasing radius near the center. This variety suggests that clusters today are still in a variety

of dynamical states and that indiscriminately combining a set of clusters to improve the statistics can easily lead to incorrect results if clusters with different kinematics are averaged together. Even within a single cluster, it is important to discriminate between the generally red, virialized population and the newly infalling bluer galaxies; including the latter in steady state kinematical analyses will artificially inflate the mass estimate; we suggest that this effect accounts for the mass of $5.77^{+1.80}_{-1.50} \times 10^{14}\ h^{-1}\ M_{\odot}$ derived for AWM 7 by Girardi et al. (1998).

In principle, the nonvirialized Em galaxies can be used as tracers of the escape velocity to arrive at an independent mass measurement (Diaferio & Geller 1997; Diaferio 1999). In practice, there are not enough Em galaxies in our sample for this method to yield a robust mass estimate; although the formal mass returned by this method for AWM 7 (kindly computed for us by A. Diaferio) is comparable to the ones we derive here, the fractional error in that mass is ~ 0.9.

Our enlarged sample confirms the presence of a cold core in the cluster (Koranyi et al. 1998); although still noisy near the cluster center, the velocity dispersion within a projected radius of $\sim 0.2\ h^{-1}$ Mpc is lower than in the range 0.2–0.5 h^{-1} Mpc. Beyond $\sim 1\ h^{-1}$ Mpc the velocity dispersion drops below the range in the core. Abell 576 (Mohr et al. 1996), a similarly well-sampled cluster, has a more pronounced cold core but a rising absorption-line velocity dispersion profile in the range 0.4–1.2 h^{-1} Mpc. A simple dynamical argument suggests that cold cores arise naturally from the NFW density profile. Assuming virial equilibrium to hold in the core, $\sigma^2 \propto GM(<r)/r$. Modeling the density profile at small radii as a power law $\rho(r) \propto r^{-\alpha}$ yields $M(<r) \propto r^{3-\alpha}$, so $\sigma \propto r^{1-\alpha/2}$. For the NFW profile, $\alpha = 1$ in the core, resulting in a rising velocity dispersion profile.

Because the velocity dispersion profile, mass profile, and orbital anisotropy profile are coupled through the Jeans equation, it is difficult to derive a mass profile without making some assumptions about the form of one or more of these functions along the way. The projected velocity dispersion profile is directly observable, but it is sensitive to outliers and substructure and requires either extensive smoothing or a large number of galaxies for a robust determination. The anisotropy profile is also difficult to constrain, with some evidence for a variety of profiles possible in clusters (Girardi et al. 1998). The mass profile can be estimated from X-ray observations, but these tend to have few data points, large errors, and cover only the inner regions of clusters; consequently, they can be fit by a wide range of models, resulting in large uncertainties in mass when extrapolated to large cluster radii.

It seems difficult to avoid circular logic in computing the surface term, as it depends on both the anisotropy profile and the density distribution that one is trying to determine. One can make a self-consistency argument, as we do here, to verify that the assumed density profile used to correct the virial mass profile agrees with the virial profile so corrected; if the surface term were small, this circularity would be less troublesome, because the assumed density profile would affect the virial mass profile only through that small correction. However, as Figure 6 illustrates, the surface term correction is often significant, particularly at small radii. Not only is the correction large, but it is also uncertain, sensitive to uncertainty in the anisotropy profile alone. The coupling between the mass profile and the surface term is thus quite strong; even with the assumption of a density profile (which in principle renders the whole exercise redundant because the mass profile is then already known), the surface term correction is too poorly constrained to produce a reliable mass profile. Only at the edges of the cluster does the surface term correction become reliable, but by then it is no longer very important. Accurate determination of cluster masses from the virial estimator, then, requires broad angular coverage; dense sampling of the core is not enough.

7. CONCLUSION

We derive the mass profile of AWM 7 in two independent ways from an optical sample of 179 galaxies with redshifts within $1.7\ h^{-1}$ Mpc of the cluster center; we use only the 137 absorption-line galaxies (and a 135 element subset of them) in the analysis. One method uses the surface number density and global velocity dispersion; the other uses individual velocities and pairwise distances. Both assume an underlying NFW profile. The two methods yield remarkably consistent mass estimates, particularly at the outer limit of our sample; the enclosed mass within a projected radius of $1.7\ h^{-1}$ Mpc agrees within 15% for both samples. The mass estimates are sensitive to the inclusion of two outliers in the sample; both the NFW and virial masses increase by $\sim 15\%$ when they are included. Including the Em galaxies, with their larger dispersion, in the calculation results in a virial mass larger by a factor of 2. The cluster mass within $1.7\ h^{-1}$ Mpc is $\sim (3 \pm 0.5) \times 10^{14}\ h^{-1}\ M_{\odot}$.

The surface term correction to the virial mass estimator is sensitive to noise in the velocity dispersion profile and to the assumed velocity anisotropy profile. The surface term at small radii is too unreliable for the virial mass estimator to be used for measuring mass profiles; at large radii, where the surface term is more certain, it is no longer an important correction to the enclosed mass. The virial mass estimator is thus reliable for measuring total cluster masses but not enclosed mass profiles; to overcome the limitations of the surface term at small radii, cluster redshift samples must have broad angular coverage. Dense sampling of cluster cores can reduce the scatter in the surface term if there are enough galaxies in the core, but our experience with AWM 7 (22 cluster members among 154 Hydra redshifts) suggests that telescope time is better spent probing the outskirts of the cluster.

Untangling the relation among the anisotropy profile, velocity dispersion profile, and density profile in cluster cores may ultimately require high-resolution simulations that track both dark matter particles and, once they have formed, galaxies.

We thank Jim Peters, Perry Berlind, and Mike Calkins for obtaining many of the FAST spectra reported herein, and Susan Tokarz for preliminary reductions. We thank Mike Kurtz and Doug Mink for advice in reducing the Hydra spectra, Norman Grogin and Andisheh Mahdavi for useful discussions, and Antonaldo Diaferio for lucid discussions and for running our data through his caustic-finding algorithm. This work is supported by the Smithsonian Institution.

REFERENCES

Adami, C., Biviano, A., & Mazure, A. 1998, A&A, 331, 439
Albert, C., White, R., & Morgan, W. 1977, ApJ, 211, 309
Bahcall, J. N., & Cen, R. Y. 1992, ApJ, 398, L81
Bahcall, J. N., & Sarazin, C. L. 1977, ApJ, 213, L99
Bartelmann, M., Narayan, R., Seitz, S., & Schneider, P. 1996, ApJ, 464, L115
Binney, J., & Mamon, G. A. 1982, MNRAS, 200, 361
Binney, J., & Tremaine, S. 1987, Galactic Dynamics (Princeton: Princeton Univ. Press)
Carlberg, R. G., et al. 1997, ApJ, 476, L7
Cole, S., & Lacey, C. 1996, MNRAS, 281, 716
Crone, M. M., Evrard, A. E., & Richstone, D. O. 1994, ApJ, 434, 402
Danese, L., De Zotti, G., & di Tullio, G. 1980, A&A, 82, 322
Dell'Antonio, I. P., Geller, M. J., & Fabricant, D. G. 1995, AJ, 110, 502
den Hartog, R., & Katgert, P. 1996, MNRAS, 279, 349
Diaconis, P., & Efron, B. 1983, Sci. Am., 248, 116
Diaferio, A. 1999, MNRAS, 309, 610
Diaferio, A., & Geller, M. J. 1997, ApJ, 481, 663
Dressler, A. 1980, ApJ, 236, 351
Eke, V. R., Cole, S., & Frenk, C. S. 1996, MNRAS, 282, 263
Fabricant, D. G., Cheimets, P., Caldwell, N., & Geary, J. 1998, PASP, 110, 79
Geller, M. J., Diaferio, A., & Kurtz, M. J. 1999, ApJ, 517, L23
Girardi, M., Giuricin, G., Mardirossian, F., Mezzetti, M., & Boschin, M. 1998, ApJ, 505, 74
Huchra, J. P., & Geller, M. J. 1982, ApJ, 257, 423
Huss, A., Jain, B., & Steinmetz, M. 1999, ApJ, 517, 64
Kaiser, N. 1987, MNRAS, 277, 1
Koranyi, D. M., Geller, M. J., Mohr, J. J., & Wegner, G. 1998, AJ, 116, 2108
Kurtz, M. J., & Mink, D. 1998, PASP, 110, 934
Loeb, A., & Mao, S. 1994, ApJ, 435, L109
Loewenstein, M., & Mushotzky, R. F. 1996, ApJ, 471, L83
Mahdavi, A., Geller, M. J., Böhringer, H., Kurtz, M. J., & Ramella, M. 1999, ApJ, 518, 69
Markevitch, M., & Vikhlinin, A. 1997, ApJ, 474, 84
Mohr, J. J., Evrard, A. E., Fabricant, D. G., & Geller, M. J. 1995, ApJ, 447, 8
Mohr, J. J., Geller, M. J., Fabricant, D. G., Wegner, G., Thorstensen, J., & Richstone, D. O. 1996, ApJ, 470, 724
Navarro, J. F., Frenk, C. S., & White, S. D. M. 1995, MNRAS, 275, 720
———. 1996, ApJ, 462, 563
———. 1997, ApJ, 490, 493
Neumann, D. M., & Böhringer, H. 1995, A&A, 301, 865 (NB)
Press, W. H., Flannery, B. P., Teukolsky, S. A., & Vetterling, W. T. 1992, Numerical Recipes: The Art of Scientific Computing (2d ed.; Cambridge: Cambridge Univ. Press)
The, L. S., & White, S. D. M. 1986, AJ, 92, 1248
Webster, R. L. 1985, MNRAS, 213, 871
White, S. D. M., Navarro, J. F., Evrard, A. E., & Frenk, C. S. 1993, Nature, 366, 429
Zwicky, F. 1933, Helvetica Phys. Acta, 6, 110